Research Article ISSN 2639-9466

Nanotechnology & Applications

Porosity Determination and Characterization of Binder Jet Printed Structural Amorphous Metal (SAM) Alloy Parts Using X-Ray CT

Amamchukwu B. Ilogebe[1*], Benedict Uzochukwu[2], and Amy M. Elliot[3]

[1]*North Carolina A&T State University, US.*

[2]*Virginia State University, US.*

[3]*Oak Ridge National Laboratory, US.*

[*]Correspondence:
Amamchukwu B. Ilogebe, North Carolina A&T State University, US.

Received: 04 November 2019; **Accepted:** 29 November 2019

Citation: Amamchukwu B. Ilogebe, Benedict Uzochukwu, Amy M. Elliot. Porosity Determination and Characterization of Binder Jet Printed Structural Amorphous Metal (SAM) Alloy Parts Using X-Ray CT. Nano Tech Appl. 2019; 2(1): 1-6.

ABSTRACT

The advent of Binder jet additive manufacturing continued to a revelation in the manufacture of intricate metal parts. This technology has been utilized in medical, aerospace and automotive industries, not much has been reported in the printing of parts from amorphous metal powders, which have found numerous applications in engineering because of their special properties. In this research, special emphasis was placed on two different manufacturing methods for structural amorphous metal alloy (SAM alloy); Die compaction and Binder jet printing. Samples of SAM alloy was created from these two-manufacturing methods and were subsequently, sintered, analyzed and compared. Previous studies show that as much as up to 50% porosity could be recorded in binder jet printing [1,2]. In this regard, different techniques were used to determine the percentage porosity from both manufacturing methods. The Archimedes method was used to determine the density and percentage porosity of the parts from the two methods. Similarly, percentage porosity was also determined using different tools in computed tomography (CT) analysis. The porosity results from both methods show good agreement. Finally, a range of applied pressure for the die compaction method was determined, at which the percentage porosity is the same as in the parts manufactured through binder jet printing.

Keywords

Binder-jet Printing, Additive Manufacturing, Porosity, Density, Die-compaction, Amorphous metal.

Introduction

Additive manufacturing (AM), also known as 3D printing, is emerging as a promising method for the fabrication of complex 3D structures and has the potential to replace the conventional techniques used in the manufacture of commercial devices based on advanced materials [3], as well as offering a promising alternative to the conventional injection molding method to fabricate near-net-shaped magnets [4]. The production of parts through metal powder compaction has been remarkable, but most times requires postprocessing. An example of such postprocessing activity is machining, which poses a major problem due to the high hardness of these materials [2]. To avoid potentially required post-processing activity, binder-jet 3D printing can be utilized in the production of intricate parts. Research has shown that parts printed from binder-jet printing possess low densification, which is exceptionally important in manufacturing parts for bioimplants, automotive and aerospace industries as they often require materials that possess high strength to weight ratio. Bram et al. suggested that high strength to weight ratio can be achieved in high porosity titanium, stainless steel and superalloy parts [5]. In other circumstances where high densification is needed, the part manufactured is subjected to liquid metal infiltration [2].

Binder jet 3D printing is an additive manufacturing method in which powder is deposited layer-by-layer and selectively joined in each layer with a binder. Since the powder does not melt during printing, the density after printing is about 50%, and sintering is needed to densify as-printed parts [1]. Binder jet 3D printing process follows the opposite principles of subtractive manufacturing which utilizes material-removal processes such as milling, drilling, etc. to manufacture 3D parts [6].

3D printing has a wide range of applications in medicine, education, aerospace industries, automotive industries, etc. In medicine, rapid

and convenient customized implants can easily be manufactured. Researchers have manufactured patient-specific mandibular implants in maxillofacial surgery [7-9], cranial vault implants for cranioplasty in neurosurgery [10,11], hip implants in orthopedic surgery [12,13], and a bioresorbable airway splint for complex tracheobronchomalacia in pediatric cardiothoracic surgery [14]. In addition to medical applications, 3D-printed haptic bio-models can be useful for educating patients during medical consultations and training surgical trainees [15-20]. Figure 1 displays data generated by Cotteleer and Joyce in 2013 which shows additive manufacturing systems deployments by application.

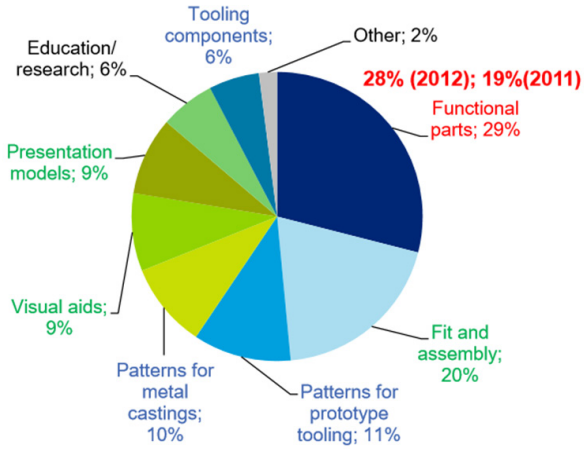

Figure 1: AM systems deployments by applications [23].

The usefulness of AM cannot be overemphasized, neither is the economic impact on society. AM technology has continually gained ground in automotive, medical and aerospace industries as they lead the revenue by 43% as shown in figure 2.

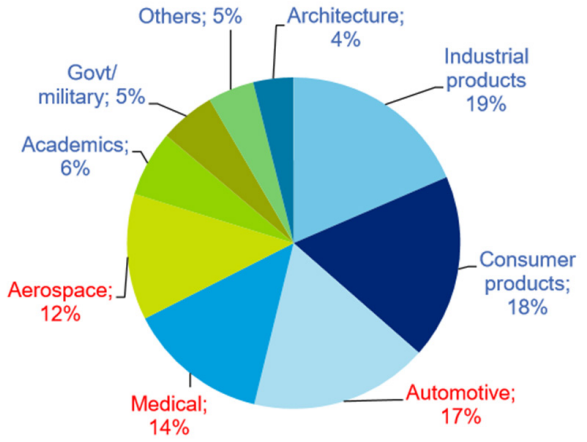

Figure 2: AM system sales revenue to various sectors [23].

However, Binder jet additive manufacturing printers are very expensive that many research laboratories could not afford it, but rather depend on other bigger laboratories [2]. This was the case with the "Advanced Metallic Materials and Porous Structure" research laboratory which solely depends on Oak Ridge National Laboratory for binder jet printing of their samples. For this reason, this research was conducted to compare the properties of parts manufactured through binder jet printing and die pressing, considering porosity and density as the intriguing properties.

Structural amorphous metal (SAM) alloys differ from traditional carbon steels in that they have non-crystalline structure and possess unique physical and magnetic properties that combine strength and hardness with flexibility and toughness. Unlike carbon steels, SAM alloys have high resistance to corrosion and wear [21,23].

Material

This research was conducted on Structural Amorphous Metal (SAM) Alloy as received from Oak Ridge National Laboratory. The first step was to characterize the powder. The morphology of the as-received rapidly-solidified powder has different shapes and various particle sizes as shown in figure 3.1. This alloy was designed such that when heated, thermally-stable carbides and borides precipitate and prevent grain growth [24]. The SAM alloy powder was sieved to remove particles larger than 45µm which can interfere with printing and or cause large pores in the samples. The composition of the powder is shown in table 1, and the morphology is shown in figure 3.

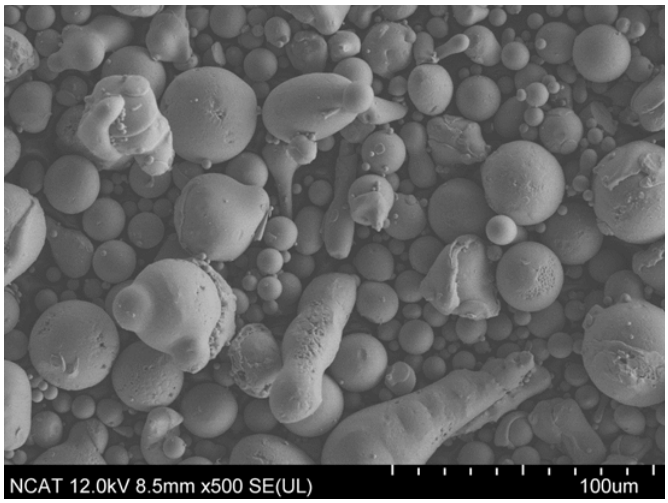

Figure 3: Morphology of SAM alloy powder.

Element	Fe	Cr	Mo	V	B	C	Si	O
Composition (wt.%)	49.38	18	16	8.9	3.4	3.3	1.0	0.02

Table 1: Composition in wt. % of SAM alloy powder.

Binder Jet Printing

The 3D printing process can be divided into three stages. The virtual model is first created using computer-aided design (CAD) software. This can also be created using a three-dimensional scanner, as well as through photogrammetry where the model is obtained by combining several images of the object taken from different angles [25]. The CAD model is converted to the .STL file (stereolithography), and the information of the model's surface is stored as a list of coordinates of triangulated sections. 2D cross-sectional layers are then generated by converting the .STL file into slices, which is recognized by the 3D printer. Finally, the part is built by depositing powders and a binder on top of each other until the last slice is printed.

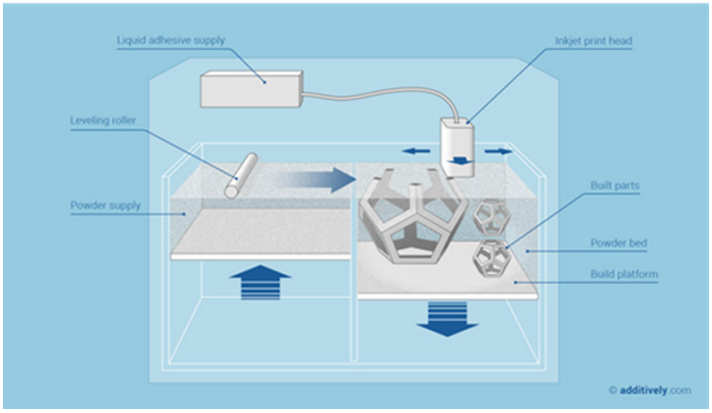

Figure 4: Schematic diagram of a binder jet system.

Die Compaction

The SAM alloy powder was sieved with 45µm wire mesh sieve (likewise in binder jet printing), weighed and thoroughly mixed with polyvinyl alcohol as a binder. The mixed powder was used to make green samples, by subjecting various samples to different loads. The applied pressure was obtained using the equations below;

$$Pressure, P = \frac{Force, F}{Area, A} \quad 1$$

$$\text{and } A = \pi r^2 \quad 2$$

Where r, r is the radius of the cylindrical green sample.

Ten samples were created under different applied pressure, while density and porosity were determined and compared to the result obtained from the binder jet printer samples.

Density Measurement

Density is a measure of mass per unit volume of a substance. The density of the samples was determined using 10 samples, each from the binder jet printed samples and die-compacted samples. Density measurement was calculated using equations 3;

$$\rho = \frac{M}{V} \quad 3$$

Where M = mass and V = volume.

Furthermore, the density of the samples was determined using Archimedes principle. The masses were measured. The measurements were done on-air and in fluid (water). Thus, the density of the samples, ρ_{sample} was calculated using equation 4 as follows [26];

$$\rho_{sample} = \frac{m_{air}\rho_{fluid}}{m_{fluid}} + \rho_L \quad 4$$

Where m_{air} and m_{fluid} are mass of sample in air and fluid respectively, while ρ_{fluid} is the density of water and ρ_L is the air buoyancy (ρ_L = 0.0012g/cm^3) [27].

Similarly, the Archimedes method of determining the porosity of a material is a classic method that has been used previously for determining the density of materials manufactured through additive manufacturing methods. One of the advantages of the Archimedes method is that it is relatively easy to carry out with a commercial instrument. However, samples with surface breaking pores or cracks that allow for water-infiltration may result in an error in measurement.

$$\phi_a = \frac{W_{sat} - W_{dry}}{W_{sat} - W_{sub}} \quad 5$$

Where ϕ_a is the Archimedes porosity, W_{sat} is the weight of the saturated samples, W_{dry} is the weight of the dry samples and W_{sub} is the weight of the submerged sample.

Computed Tomography (CT)

Computed Tomography of the samples which gives a 3D structural analysis in a non-destructive way, visualizes both the material composition and its internal architecture at the microscopic level. Scans were performed with a phoenix nanotom m. The processes involved in CT operation includes scanning, capturing, reconstruction, and volume analysis. This was used to determine the percentage volume of material and percentage porosity in the samples. The X-ray tube voltage for the scan was set to 130kV and the current to 50µA, while a long scan time of 3 hours was achieved to alleviate noise and improve image quality. During one scan, 2400 radiographic projections were taken over a 360° rotation. The exposure time was set to 500ms, and an isotropic voxel size of 6 x 6 x 6 µm was achieved. The Phoenix datos|x software was used to reconstruct the X-ray CT scans and to export cross-sectional images [28]. These were employed to analyze the sintered samples, as well as determine the percentage porosity in both binder jet printed samples and die pressed samples.

Computed tomography was used for 3D analysis and also to validate results obtained from other characterization techniques. Images are separated by color greyscale or position or both. The algorithms typically utilize these principles of greyscale and positioning. In addition, isolation by greyscale (also called segmentation or thresholding) is crucial to much of the CT analysis.

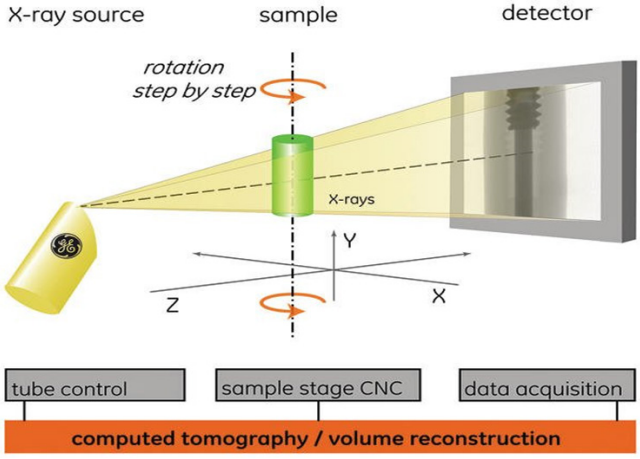

Figure 5: Schematic diagram of Computed Tomography operational process.

However, conventional CT systems have constraints in sample sizes. This contributes to the difficulties encountered in CT

processes; in some cases, it has become impossible to image large-scale samples. This limitation prohibited the successful analysis of the sample size used, as these samples were cut before imaging. Another constraint with CT analysis is the difficulty or sometimes the inability to determine the internal structure of materials (as observed in highly dense materials).

In this research, the material was isolated by performing a Surface Determination. This was done manually and automatically with computer assistance. The latter was done for comparison of results from the former, to ensure consistency. This procedure involved the definition of the porous region as the "background" and the scene as the "material". The program averages the greyscales in each of these regions and picks a greyscale value to be a background and one to represent material. It then picks the greyscale halfway between these values and this is known as an "iso 50-50".

The volume analyzer and defect detector technique were also used to validate the results obtained from surface determination. These were used to ascertain the volume of pores in the sintered samples from binder jet printing and die compaction.

Results and Discussion

Density and Porosity

The results from density measurement and calculation were obtained and presented in the graph in Figure 6. There was a disparity in percentage porosity from samples produced through binder jet printing and those from die-compaction at certain applied pressures. Die compacted samples exhibit higher porosity when the applied pressure is below 600MPa, whereas at 608MPa to 688MPa, the percentage porosity from both manufacturing methods was relatively consistent. Furthermore, the porosity tends to decrease when 700MPa or more is applied for the traditional die compaction method, making the powder particles to be more closely packed.

Similarly, the density of the samples from both the manufacturing method followed the same trend as porosity. The binder jet samples have an average density of 3.96g/cm^3, while the samples from die-compaction averaged out to 4.05g/cm^3 after 10 samples from both manufacturing methods were analyzed. The die compacted samples were for density determination were obtained between 610MPa and 700MPa.

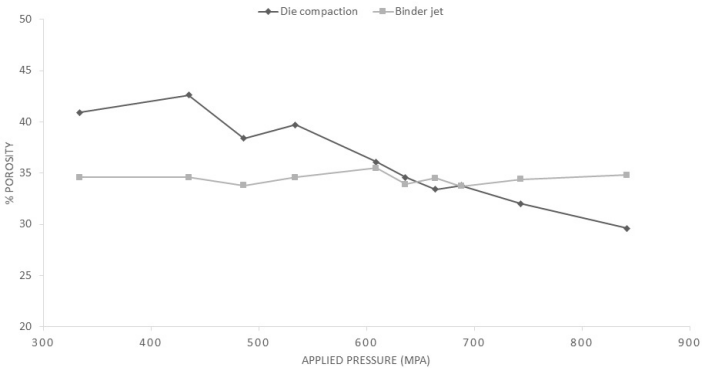

Figure 6: Plot of percentage porosity for die compacted and binder jet printed samples. (No pressure applied in binder jet method).

Computed Tomography (CT)

Computed tomography results show a tremendous level of consistency throughout the techniques employed in the analysis. The samples were first sectioned by choosing the regions of interest (ROI) and extracting them for analysis. This also helped to reduce the duration of analysis and optimization of results, especially with high opaque materials as observed with SAM alloy.

The sintered samples recorded porosity within the range of 32.17% to 36.38%. The porosity as recorded from the volume analyzer on the die compacted sample was 34.05% as shown in figure 7, while wall thickness tool analysis shows 34.66% porosity on the binder jet printed sample (Figure 8). These tools were designed to detect the porous sites in the material. On the other hand, the percentage of the material in the binder jet sample was also determined using a volume analyzer and was found to be 67.83% as shown in figure 9. The balance of 32.17%, is percentage porosity and can be compared to the results obtained from wall thickness and volume analyzer of the porosity.

Other CT tools employed for porosity measurement includes surface determination and defect detector. The results from all the techniques were collected and tabulated as shown in table 2.

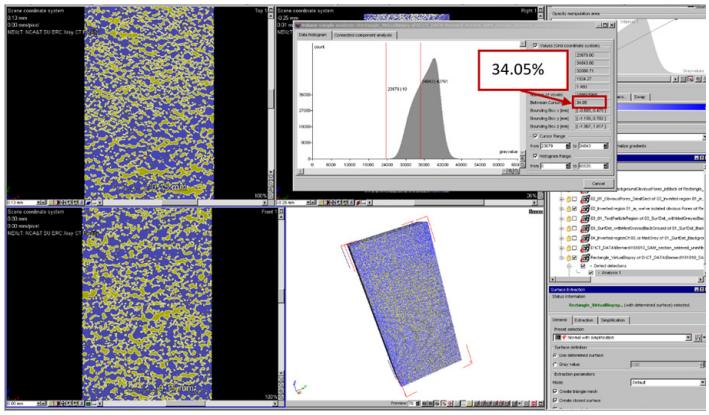

Figure 7: Pores analysis of the sintered sample using volume analysis on a die-compacted sample.

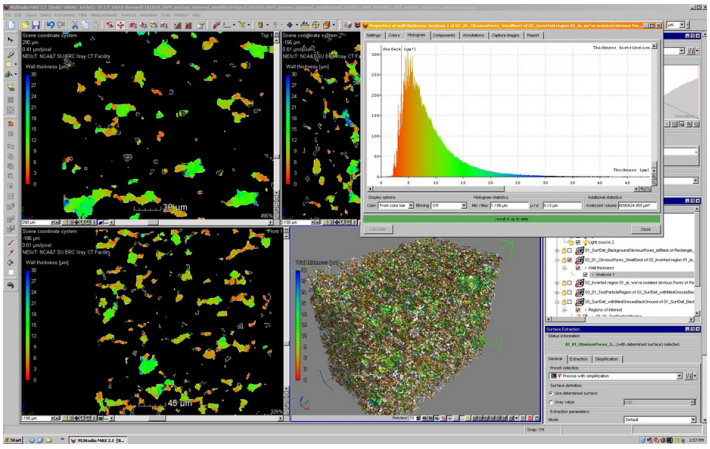

Figure 8: Wall thickness analysis from the sintered samples.

	Archimedes	Surface Determination	Wall Thickness	Volume Analyzer (pores)	Volume Analyzer (Material)	Defect Detector
Binder Jet	34.5	35.08	34.66	36.17	32.17	36.38
Die compaction	33.4	36.38	33.47	34.05	32.82	35.43

Table 2: Results from different techniques of porosity determination.

Conclusion

In this paper, a range of applied pressure necessary for die-compacted parts to have the same structural properties as the parts from binder-jet printing has been presented. Thus, one can model binder-jet printed parts using the die-compaction technique, especially as the binder jet printers are not easily affordable by most research institutions. On the other hand, it is challenging to scan high opaque materials in the CT scanners, as poor images caused by noise are common with these types of materials. However, poor CT-images caused by noise at lower energies could be outmaneuvered by increasing scanning time, which was necessary for this research. Similarly, CT-artefacts such as beam hardening, which seems to have a tremendous effect on phase discrimination was averted using filters [29].

Acknowledgment

We acknowledge the support from Dr. Boyce Collins for the training received on the CT scan machine. We also acknowledge the support provided by the National Science Foundation Award #0959511: "MRI-R2: Acquisition of a Nanotom Computed Tomography System for Revolutionizing Metallic Materials Research for education and training. We equally want to thank the Oak Ridge National Laboratory for their unalloyed support with binder jet printing.

References

1. Mostafaei A, Erica L. Stevens, Eamonn T. Hughes, et al. Powder bed binder jet printed alloy 625: Densification, microstructure and mechanical properties. Materials & Design. 2016; 108: 126-135.
2. Amamchukwu B. Ilogebe, Cynthia K. Waters, Amy M. Elliot, et al. Morphology of Binder-Jet Additive Manufactured Structural Amorphous Metal Matrix Composites. The International Journal of Engineering and Science. 2019; 8: 15-24.
3. Amir Azhari, Ehsan Marzbanrad, Dilara Yilman, et al. Binder-jet powder-bed additive manufacturing (3D printing) of thick graphene-based electrodes. Carbon. 2017; 119: 257-266.
4. Ling Li, Brian Post, Vlastimil, et al. Additive manufacturing of near-net-shape bonded magnets: Prospects and challenges. Scripta Materialia. 2017; 135: 100-104.
5. M. Bram C. Stiller H.P. Buchkremer, et al. High-porosity titanium, stainless steel, and superalloy parts. Advanced engineering materials. 2000; 2: 196-199.
6. Davim J.P. Machining: Fundamentals and Recent Advances. Springer Science & Business Media. 2008.
7. Saijo H, Igawa K, Kanno Y, et al. Maxillofacial reconstruction using custom-made artificial bones fabricated by inkjet printing technology. Journal of Artificial Organs. 2009; 12: 200-205.
8. Klammert U, Gbureck U, Vorndran E, et al. 3D powder printed calcium phosphate implants for reconstruction of cranial and maxillofacial defects. Journal of Cranio-Maxillofacial Surgery. 2010; 38: 565-570.
9. Li J, Hsu Y, Luo E, et al. Computer-aided design and manufacturing and rapid prototyped nanoscale hydroxyapatite/polyamide (n-HA/PA) construction for condylar defect caused by mandibular angle ostectomy. Aesthetic plastic surgery. 2011; 35: 636-640.
10. D'Urso PS, Earwaker WJ, Barker TM, et al. Custom cranioplasty using stereolithography and acrylic. British Journal of Plastic Surgery. 2000; 53: 200-204.
11. Wurm G, Tomancok B, Holl K, et al. Prospective study on cranioplasty with individual carbon fiber reinforced polymere (CFRP) implants produced by means of stereolithography. Surgical neurology. 2004; 62: 510-521.
12. Koulouvaris P, Stafylas K, Sculco T, et al. Distal femoral shortening in total hip arthroplasty for complex primary hip reconstruction. A new surgical technique. The Journal of arthroplasty. 2008; 23: 992-998.
13. Bicanic G, Barbaric K, Bohacek I, et al. Current concept in dysplastic hip arthroplasty: Techniques for acetabular and femoral reconstruction. World journal of orthopedics. 2014; 5: 412.
14. Zopf DA, Hollister SJ, Nelson ME, et al. Bioresorbable airway splint created with a three-dimensional printer. N Engl J Med. 2013; 368: 2043-2045.
15. Wurm G, Tomancok B, Pogady P, et al. Cerebrovascular stereolithographic biomodeling for aneurysm surgery. Journal of neurosurgery. 2004; 100: 139-145.
16. Waran V, Narayanan V, Karuppiah R, et al. Utility of multimaterial 3D printers in creating models with pathological entities to enhance the training experience of neurosurgeons. Journal of neurosurgery. 2014; 120: 489-492.
17. Watson RA. A low-cost surgical application of additive fabrication. Journal of Surgical Education. 2014; 71: 14-17.
18. Witschey WR, Pouch AM, McGarvey JR, et al. Three-dimensional ultrasound-derived physical mitral valve modeling. The Annals of thoracic surgery. 2014; 98: 691-694.
19. Abla AA, Lawton MT. Three-dimensional hollow intracranial aneurysm models and their potential role for teaching, simulation, and training. World neurosurgery. 2015; 1: 35-36.
20. Mashiko T, Otani K, Kawano R, et al. Development of three-dimensional hollow elastic model for cerebral aneurysm clipping simulation enabling rapid and low-cost prototyping. World neurosurgery. 2015; 83: 351-361.
21. Achebe C. The Effects of Inhibition on Corrosion of Mild Steel in H2SO4 Using Ethanol Extract of Vernonia Amygdalina. The International Journal of Engineering and Science. 2015; 4: 28-36.
22. Achebe CH, Amamchukwu Ilogebe, Jeremiah Chukwuneke, et al. Mild Steel Corrosion Inhibition in H2SO4 Using Ethanol Extract of Vernonia Amygdalina. The International Journal of Engineering and Science. 2014; 4: 01-09.

23. Cotteleer M, Joyce J. 3D opportunity: Additive manufacturing paths to performance, innovation, and growth. Deloitte Review. 2014; 14: 5-19.
24. Cordero Z, Elliott A. Collaboration for The Advancement of Indirect 3d Printing Technology. 2016.
25. Ambrosi A, Pumera M. 3D-printing technologies for electrochemical applications. Chemical Society Reviews. 2016; 45: 2740-2755.
26. Giancoli D.C. Physics: principles with applications, Pearson Education. 2005.
27. Urquhart A. Novel reinforced ceramics and metals: a review of Lanxide's composite technologies. Materials Science and Engineering: A. 1991; 144: 75-82.
28. Jeroen Soete, Brice Badoux, Yentl Swolfs, et al. "Defect detection in 3D printed carbon fibre composites using X-ray Computed Tomography". 9th Conference on Industrial Computed Tomography, Padova, Italy. 2019.
29. Sleutel S,V. Cnudde B. Masschaele, et al. Comparison of different nano-and micro-focus X-ray computed tomography set-ups for the visualization of the soil microstructure and soil organic matter. Computers & Geosciences. 2008; 34: 931-938.